energy&fuels

pubs.acs.org/EF

Article

Hybrid Pore-Scale Adsorption Model for CO_2 and CH_4 Storage in Shale

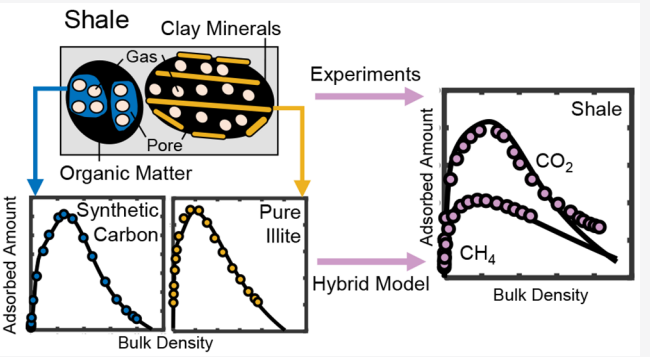
Humera Ansari, Shuwei Gong, JP Martin Trusler, Geoffrey Maitland, and Ronny Pini*

Cite This: *Energy Fuels* 2022, 36, 3443−3456

Read Online

ACCESS | Metrics & More | Article Recommendations | Supporting Information

ABSTRACT: Making reliable estimates of gas adsorption in shale remains a challenge because the variability in their mineralogy and thermal maturity results in a broad distribution of pore-scale properties, including size, morphology and surface chemistry. Here, we demonstrate the development and application of a hybrid pore-scale model that uses surrogate surfaces to describe supercritical gas adsorption in shale. The model is based on the lattice density functional theory (DFT) and considers both slits and cylindrical pores to mimic the texture of shale. Inorganic and organic surfaces associated with these pores are accounted for by using two distinct adsorbate−adsorbent interaction energies. The model is parametrized upon calibration against experimental adsorption data acquired on adsorbents featuring either pure clay or pure carbon surfaces. Therefore, in its application to shale, the hybrid lattice DFT model only requires knowledge of the shale-specific organic and clay content. We verify the reliability of the model predictions by comparison against high-pressure CO_2 and CH_4 adsorption isotherms measured at 40 °C in the pressure range 0.01−30 MPa on four samples from three distinct plays, namely, the Bowland (UK), Longmaxi (China), and Marcellus shale (USA). Because it uses only the relevant pore-scale properties, the proposed model can be applied to the analysis of other shales, minimizing the heavy experimental burden associated with high-pressure experiments. Moreover, the proposed development has general applicability meaning that the hybrid lattice DFT can be used for the characterization of any adsorbent featuring morphologically and chemically heterogeneous surfaces.



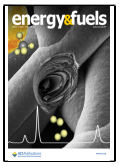
1. INTRODUCTION

Shale gas production continues to accelerate globally, along with an interest in improving recoveries from these "tight" reservoirs.[1] CO_2-enhanced shale gas recovery (ESGR) has been considered as a potential means of achieving higher production rates, while alleviating some of the impact on the climate by the permanent sequestration of CO_2 within the shale reservoir.[2,3] The underlying physical mechanism in shale that theoretically supports this technique is gas adsorption. As shales have pores that are nanometric in size,[4] gas is stored not only as compressed fluid (like in conventional reservoirs) but also as adsorbed gas at liquidlike densities.[5] Studies have shown that shale is more selective toward CO_2 compared to CH_4, the main component of shale gas.[6,7] This further indicates that the injection of CO_2 would not only lead to operational benefits, such as maintenance of the reservoir pressure, but also promote desorption and recovery of CH_4.[8,9]

When evaluated as sorbent material, shale can be represented as composed of pores found in the organic (i.e., kerogen) and inorganic (i.e., clay minerals) components of the rock matrix.[10,11] Although these two components may show a similar distribution of (equivalent) pore sizes,[12,13] they differ substantially in terms of surface chemistry and pore morphology. Clay minerals are usually stacked and layered[14] and form slitlike, elongated pores, while the organic matter features curved and spherical pores.[4,15,16] Making reliable estimates of gas adsorption on shale can be challenging due to the natural variability in their mineralogy and thermal maturity, in addition to a wide distribution of pore sizes.[17] Models that can predict this behavior based on selected textural and chemical properties of a given shale would be highly beneficial in limiting the experimental burden associated with both characterization and high-pressure adsorption measurements. Once developed, such predictive models could become integral to workflows for resource evaluation.

Models typically used to describe supercritical gas adsorption on shale vary in their complexity. By far the most commonly used models, particularly for CH_4 adsorption, are empirical ones, such as those based on the Langmuir or BET isotherm equations.[18−20] These models have been derived for

Received: November 1, 2021
Revised: February 14, 2022
Published: March 12, 2022



Downloaded via IMPERIAL COLLEGE LONDON on May 11, 2022 at 07:45:00 (UTC).
See https://pubs.acs.org/sharingguidelines for options on how to legitimately share published articles.

ACS Publications

© 2022 American Chemical Society

subcritical or vapor adsorption. Their extension to high pressures means that many of their underlying assumptions need to be ignored or that some parameters lose their physical meaning. Additionally, in their application to supercritical adsorption, these models require making assumptions on the magnitude and the behavior of either the volume or the density of the adsorbed phase as a function of pressure.[21] As a consequence of their simplicity, they are also often unable to capture the complex, pore-size-dependent adsorption behavior that is typical of micro-/mesoporous adsorbents.[22] Molecular simulations have been widely adopted to describe adsorption in clay minerals, organic pores, and shales.[23−25] The most common approaches include Grand Canonical Monte Carlo (GCMC),[26] density functional theory (DFT),[27] lattice Boltzmann methods,[28,29] molecular dynamics (MD) simulations,[30] and pore network modeling.[31] Although these models vary in their complexity, their application can often be restricted to small, simple domains (single pore systems with simplified pore geometries). The development of multitechnique approaches[32−35] is particularly promising for the most realistic description of gas storage *and* transport in shale. While they provide useful insight into the adsorption process on a molecular level,[36] these numerical approaches remain computationally expensive, requiring the application of parallel computing to offset this cost, as has been successfully demonstrated for lattice Boltzmann methods.[28,29] Pore-scale numerical approaches, such as the lattice density functional theory (lattice DFT), have been shown to be a practical, yet physically sound, compromise for the description of supercritical gas adsorption in porous solids.[37,38] The lattice DFT model incorporates the pore size distribution of the adsorbent to describe the adsorption behavior on a pore-by-pore basis, and it explicitly accounts for adsorbate−adsorbate and adsorbate−adsorbent interactions. Although this numerical approach has been applied to a wide range of natural sorbents,[39−41] its application to shale is still in its infancy.

In this paper, we develop a hybrid adsorption isotherm model for adsorbents featuring pores with distinct shapes and surface chemistries, such as shale. The model is based on the lattice DFT, and it considers slit as well as cylindrical pores to mimic the texture of shale. The organic and inorganic surfaces in shale are accounted for by using two distinct adsorbate−adsorbent interaction energies. The parameters of the model are obtained independently by using experimental adsorption data acquired on adsorbents featuring either pure clay or carbon surfaces. Therefore, the application of the model to shale only requires knowledge of the shale-specific organic and clay content. The reliability of the model predictions is verified by comparison against high-pressure CO_2 and CH_4 adsorption isotherms measured on four samples from three important shale plays.

2. MATERIALS

2.1. Shale Samples. The samples used in this study have been retrieved from three main shale plays: the (i) Bowland shale (UK), (ii) Longmaxi shale (China), and (iii) Marcellus shale (USA). These shales were selected due to their importance in the wider shale gas industry and the substantial effort that has gone into characterizing them. The Marcellus shale is the largest shale play in the USA[42] and has about 135 trillion cubic feet of proved reserves.[43] The Longmaxi shale in the Sichuan Basin is one of the key targets in China,[44] with the Fuling area currently being the largest producing reservoir in the country.[45] In the UK, although shale gas exploration is in its infancy, the Bowland shale is considered a prime target for production.[46]

The Bowland shale samples (labeled as B1, B2, B5, B6, B8, and B13) come from the Preese Hall-1 well in the lower Bowland shale formation.[47] Sample ML has been obtained from a well in the postmature part of the Marcellus shale in the northeast of Pennsylvania.[48] The Longmaxi shale samples (LG3, LG4, and LG5) were retrieved from sections WX-1, WX-5 (in the same well), and WX-7 (in another well) in the Jiaoshiba area (Fuling gas field) and Dingshan area (west of Fuling), respectively.[49] The mineralogy of all samples is reported in Table S1, and details on the associated experimental procedures can be found in the publications listed above. The samples are composed of a variety of clay minerals, and they differ in both their organic content and degree of thermal maturity. The Marcellus and Bowland shales have a maximum vitrinite reflectance of approximately 4.0%[48] and 1.1%,[46] respectively, and the Longmaxi shales have an equivalent vitrinite reflectance (as they are vitrinite-free) of approximately 3.3−4.6%.[49] This is also reflected in their visual appearance: the B samples are light gray, while ML and LG samples are much darker and almost black. All shale samples were prepared for the study by crushing and sieving to below a 100 μm particle size. Although all samples were used for textural characterization, only four of them (B6, B8, ML, and LG4) have been selected for the high-pressure adsorption experiments. The mineralogy of these four samples is reported in Table 1.

Table 1. Mineralogy in wt% of Samples B6, B8, ML, and LG4 Used in the Supercritical Gas Adsorption Studies[a]

	Bowland shale		Longmaxi shale	Marcellus shale
component	B6	B8	LG4	ML
kaolinite	1.1	2.3		
illite/mica	17.2	19.2	18.0	45.0
illite/smectite mixed layer	5.1	trace		
smectite	0.0	4.0		
chlorite			3.0	2.0
total clays	**23.4**	**25.5**	**21.0**	**47.0**
quartz	46.1	50.2	60.0	29.0
calcite	7.2	8.6	1.0	6.0
dolomite/ankerite	trace	8.6	2.0	
siderite	0.0	0.0		
marcasite	0.9	0.6		
pyrite	8.4	2.2	3.0	7.0
albite	trace	1.2	10.0	11.0
orthoclase	1.2	2.1	3.0	
gypsum	8.6	0.0		
anatase	0.6	0.0		
TOC	3.6	0.9	7.8	6.1

[a]Data have been obtained from the following references: B6/B8, unpublished measurements from University College London; LG4, Delle Piane et al.;[49] and ML, Delle Piane et al.[48]

2.2. Reference Adsorbents. Three additional adsorbent materials were selected as part of this study to represent key features associated with the texture and surface chemistry of shale for modeling purposes. Graphitized mesoporous carbon (MC, powder, 45 ± 5 μm particle size) and microporous activated charcoal Norit (AC, RB3, 3 mm rods) were chosen as the surrogates for carbon surfaces found in the shale's meso- and micropores. Illite (IL, IMt-2, as supplied from the Clay Minerals Society) was chosen to represent the clay pores, this being the dominating clay mineral in this assortment of shales (Table 1). These materials have been extensively characterized in our previous publications,[50,51] and the results from these works will be utilized in this study.

https://doi.org/10.1021/acs.energyfuels.1c03723
Energy Fuels 2022, 36, 3443−3456

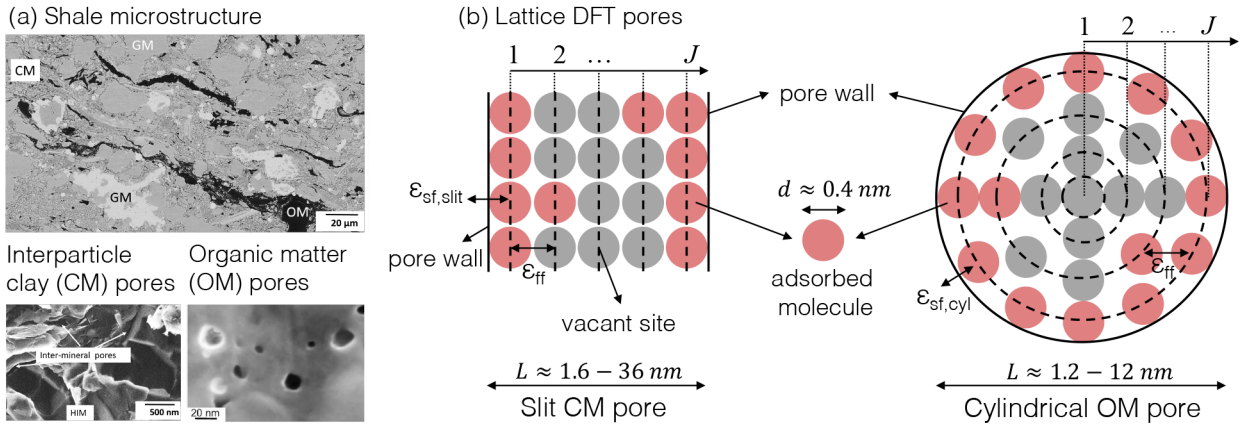


Figure 1. (a) Exemplary shale microstructure. Top: SEM image of a Bowland shale sample showing a distribution of granular material (GM), clay minerals (CM), and organic matter (OM). Bottom-left: intermineral clay pores in the same sample (imaged by helium ion microscopy). Images used in unmodified form from Ma et al.,[4] licensed under CC BY 3.0 (full terms available at https://creativecommons.org/licenses/by/3.0/legalcode), reproduced with permission from ref 4. Copyright 2021 Royal Society of Chemistry. Bottom-right: SEM image of round pores in the organic matter of a sample from the Barnett shale. Image used in unmodified form from Loucks et al.,[15] reproduced with permission from ref 15. Copyright 2009 Society for Sedimentary Geology. (b) Representation of a slit CM pore and a cylindrical OM pore in the lattice DFT framework. The size L of each pore is defined by the total number of lattice layers J and the diameter of the adsorbate molecule d. Each circle is a site in the lattice, which can be either vacant (gray) or occupied by an adsorbed molecule (red). Fluid−fluid and fluid−surface interactions are described with an interaction energy parameter (ε_{ff} and ε_{sf}).

2.3. Gases. Gases for this study were sourced from BOC, namely, CO_2, Ar, and He at purities of 99.999% and N_2 at a purity of 99.9992%; for the supercritical adsorption experiments, CO_2 and CH_4 were purchased at a purity of 99.995% and 99.5%, respectively. The critical properties of the pure adsorbates are as follows: $T_c(CO_2)$ = 304.1 K, $P_c(CO_2)$ = 7.37 MPa, $\rho_c(CO_2)$ = 10.62 mol/L;[52] $T_c(CH_4)$ = 190.6 K, $P_c(CH_4)$ = 4.60 MPa, and $\rho_c(CH_4)$ = 10.14 mol/L.[53]

3. METHODS

3.1. Textural Characterization. Subcritical Ar (87 K) and CO_2 (273 K) adsorption isotherms were measured on the Quantachrome Autosorb iQ instrument in the pressure range 1×10^{-7} to 1×10^{-1} MPa. For sample B13, a N_2 (77 K) isotherm was measured instead of Ar. When using Ar, temperature control was achieved using Quantachrome's CryoSync module, while for the experiments with CO_2, a liquid circulating thermostat (Julabo CORIO CD-200F) was used to control the temperature of a bath filled with a mixture of water and ethylene glycol (50 vol %). The shales were degassed in the equipment's external degassing station by applying a vacuum during the following temperature ramp: 25 °C (10 min), 60 °C (1 h), 90 °C (1 h), 120 °C (16 h). For samples B1, B2, and B5, subcritical N_2 (77 K) and CO_2 (273 K) adsorption isotherms were measured using a similar apparatus, the Micromeritics 3Flex surface characterization analyzer, which follows a very similar experimental protocol as above, with the addition of in situ degassing for 3 h prior to the measurement at 120 °C. Between 1 and 1.4 g was used for the experiments with CO_2 and about 0.2−0.4 g for the experiments with Ar (or N_2).

The obtained adsorption isotherms were used to infer textural properties of the shale samples, including the specific surface area, pore size distribution, as well as the cumulative micro- and mesopore volumes. To this end, the adsorption branch of each isotherm was interpreted using adsorption models available within the instrument's software. Namely, the nonlocal DFT (NLDFT) model for cylindrical silica pores was used for the Ar isotherms, while the Grand Canonical Monte Carlo (GCMC) or NLDFT models for carbon slit pores were used for CO_2 isotherms measured on the Quantachrome Autosorb iQ instrument. For the isotherms measured using the Micromeritics 3Flex surface characterization analyzer, the NLDFT model for carbon slit pores was used for both N_2 and CO_2 adsorption isotherms. All subcritical isotherms with the model fitting are shown in Figure S1. We note that although these models reproduce with high accuracy the measured adsorption isotherms, the chosen adsorption kernels (cylindrical silica pores *or* slit carbon pores) cannot fully capture the complexity of the shale's pore space. Here, the obtained results are primarily used as cumulative indicators of the shale's total micro- and mesoporosity.

3.2. Supercritical Adsorption Measurements. Supercritical CO_2 and CH_4 adsorption measurements were performed using a Rubotherm magnetic suspension balance (MSB) at 40 °C in the pressure range 0.01−30 MPa. The details of the experimental setup, methodology, and uncertainty analysis are described in our recent work.[50,51] Briefly, each sample was first degassed in situ under a vacuum for at least 12 h at 120 °C, which was followed by an experiment with helium at 80 °C to determine the skeletal volume of the adsorbent (Table S3). The adsorbate (CO_2 or CH_4) was then introduced into the measuring chamber, and measurements were taken at the set temperature and at different pressures, with an equilibration time of at least 90 min at each pressure step. Typically, between gases, a full regeneration was accompanied by another helium measurement. Between 1.6 and 2.7 g of shale was used for these measurements, and for all gases, points were taken in both adsorption mode (increasing the pressure in the MSB) and desorption mode (depressurizing the MSB). The measured quantities in these experiments are the bulk fluid density, ρ_b, and the excess adsorbed amount, n^{ex}.

4. MODELING

A hybrid adsorption model is developed in this study to describe the supercritical adsorption measurements of CO_2 and CH_4 on shale. The formulation of the model is based on the lattice DFT, which computes adsorption for pores of simplified geometries and by imposing a discretization of the pore space, such that the adsorbed molecules form a regular pattern. To describe the "true" material's pore size distribution, the lattice DFT model considers a reduced number of (equivalent) pore sizes, which are properly weighted to reproduce the cumulative pore volume distribution.[38] The model describes adsorption by considering both adsorbate−adsorbate and adsorbate−adsorbent interactions and can therefore be used to describe a wide spectrum of adsorption systems, including those considered in this study. Notably, a formulation of this modeling framework has been recently

https://doi.org/10.1021/acs.energyfuels.1c03723
Energy Fuels 2022, 36, 3443−3456

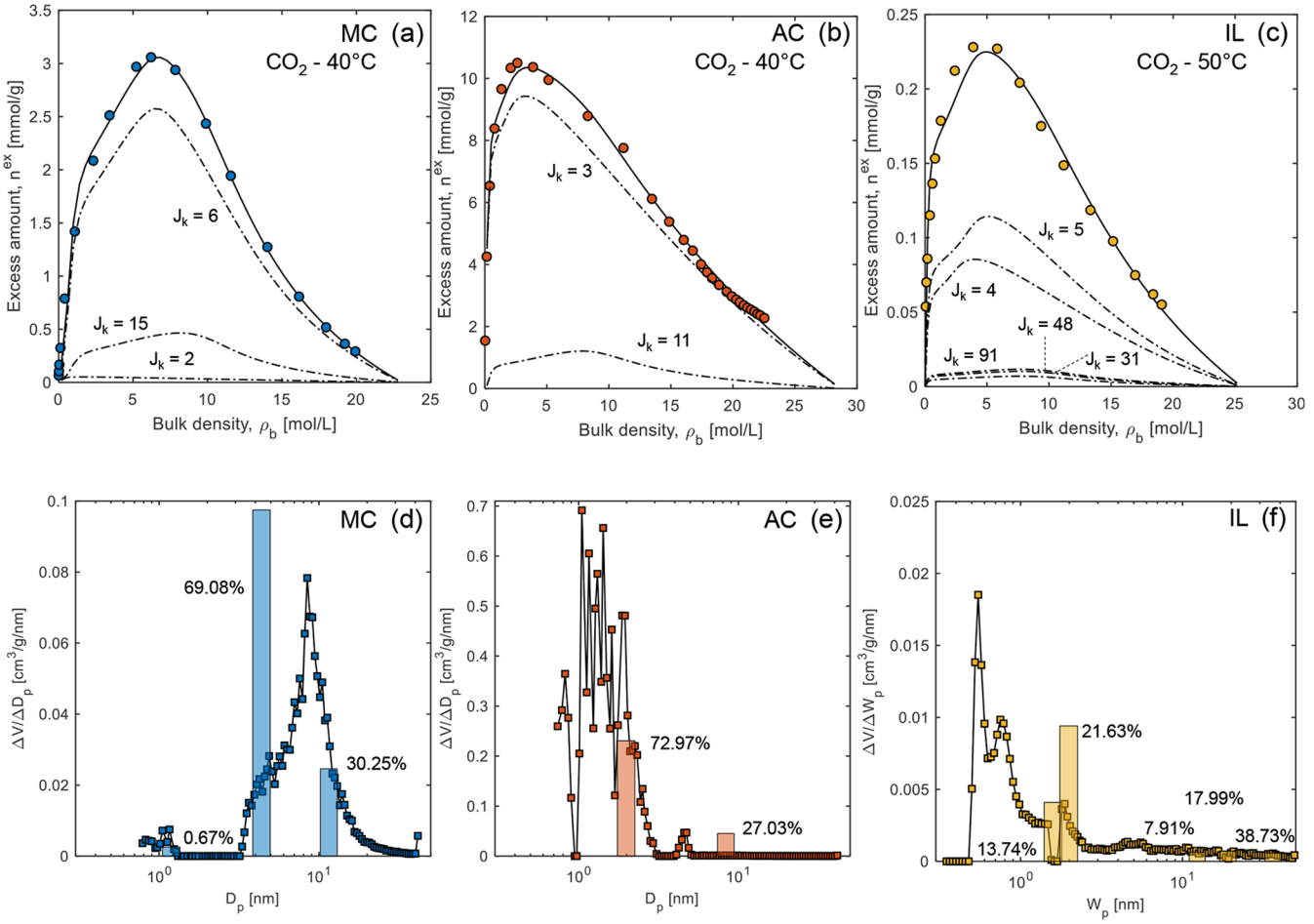


Figure 2. CO_2 adsorption isotherms for (a) MC (40 °C and cylindrical lattice DFT model, experimental data measured by Ansari et al.[50]), (b) AC (40 °C and cylindrical lattice DFT model, experimental data measured by Ustinov et al.[55]), and (c) IL (50 °C and slit lattice DFT model, experimental data measured by Hwang and Pini[51]). Symbols denote experimental data, while the solid lines are optimum fits from the lattice DFT model. The dot-dashed lines are isotherms computed for each pore class used in the lattice DFT model, with J_k being the number of lattice layers in pore class k. Pore size distribution (up to 50 nm) obtained from subcritical physisorption measurements for (d) MC, (e) AC, and (f) IL, as reported by Ansari et al.[50] (MC and AC) and Hwang and Pini[51] (IL). The bars denote the discretized PSD used in the lattice DFT model with the parameters (J_k, pore size and volume fraction) reported in Table 2.

proposed in the literature that uses two distinct adsorbate–adsorbent interaction energies to describe adsorption in micro- and meso-/macropores of shale, respectively.[41] Here, we extend this conceptualization of the shale pore space by explicitly considering the presence of clay and organic matter pores (see Figure 1a) and by accounting for differences in their shape and surface energy. Different from previous approaches, our application of the lattice DFT model to shale is predictive, as the model is independently parametrized and "calibrated" using adsorption data on surrogate surfaces, as described in the following sections.

4.1. Hybrid Lattice DFT Model. For the formulation of the hybrid lattice DFT model, the shale is divided into two distinct pore systems—slit pores and cylindrical pores—to represent voids created between clay particles and in the organic matter, respectively (see Figure 1b). The mathematical formulation for each of these pore types (i.e., the Ono-Kondo lattice equations) can be found in our previous work.[50,51] For each pore type, different pore sizes (classes) are considered in both the micro- and mesopore range. For each pore class, the numerical solution of the Ono-Kondo equations provides the lattice occupancy profile of the adsorbed fluid. In physical units, this translates into a density profile that is used to compute the excess amount adsorbed at a given temperature, T, and bulk fluid density, ρ_b, from the contribution of each individual pore class. Mathematically[50]

https://doi.org/10.1021/acs.energyfuels.1c03723
Energy Fuels 2022, 36, 3443−3456

$$n_{\text{slit}}^{\text{ex}}(\rho_b, T) = c_{\text{slit}}^{\text{sat}} \sum_{k=1}^{K} \frac{\nu_{p,k}^{\text{slit}}}{J_k} \sum_{j=1}^{J_k} (\rho_j - \rho_b)$$

$$n_{\text{cyl}}^{\text{ex}}(\rho_b, T) = c_{\text{cyl}}^{\text{sat}} \sum_{k=1}^{K} \frac{\nu_{p,k}^{\text{cyl}}}{\left[\frac{1}{4} + J_k(J_k - 1)\right]} \left[\frac{1}{4}(\rho_1 - \rho_b) + 2 \sum_{j=2}^{J_k} (\rho_j - \rho_b)(j - 1)\right] \quad (1)$$

where $n_{\text{slit}}^{\text{ex}}$ and $n_{\text{cyl}}^{\text{ex}}$ are the excess amounts adsorbed found on the clay surfaces (slit pores) and on the carbon surfaces (cylindrical pores), respectively; K is the total number of pore classes; J_k is the number of layers in pore class k; ρ_j is the density in layer j; $\nu_{p,k}$ is the specific pore volume in pore class k; and $c^{\text{sat}}(T)$ is a parameter that quantifies the fraction of the total pore space occupied by adsorbed phase at saturation. The total excess amount adsorbed for the shale is thus obtained as

$$n^{\text{ex}}(\rho_b, T) = w_c n_{\text{slit}}^{\text{ex}}(\rho_b, T) + w_o n_{\text{cyl}}^{\text{ex}}(\rho_b, T) \quad (2)$$

where w_c and w_0 are the clay and organic fraction of the shale, respectively (see Table 1). We note that the number of layers in a given pore class is the same for CO_2 and CH_4, because these two molecules have a similar molecular diameter ($d \approx 0.4$ nm). We note that the given model does not consider aspects related to the connectivity of the slit or cylindrical pores. Accounting for the structure of the pore network is key to the description of fluid transport in shale (and other porous media), which is beyond the scope of the present work that focuses on equilibrium adsorption properties.

To compute the excess amount adsorbed in each pore type (eq 1), the model described above requires the following parameters: (1) the lattice pattern, (2) the adsorbate−adsorbate interaction energy (ε_{ff}), (3) the total specific pore volume (ν_p^{tot}), (4) its discretization in a given number of representative pore classes, (5) the adsorbent−adsorbate interaction energy (ε_{sf}), (6) the theoretical maximum density in the lattice (ρ_{max}), and (7) the fraction of the total pore space occupied by adsorbed phase at saturation (c^{sat}).[50] In this study, we will use parameter values estimated upon application of the model to supercritical CO_2 and CH_4 adsorption data measured on carbon-based adsorbents (to represent the organic matter) and on illite (to represent the clay fraction), as described in next section. Therefore, by analogy with methods of pore size analysis by molecular simulation,[54] in this study, the lattice DFT excess adsorption isotherms precomputed on these surrogate pore surfaces serve as "kernels", which are combined in a proportion that reflects the composition of the given shale sample. Accordingly, the *predicted* total shale's pore volume is obtained as

$$\nu_p^{\text{tot}} = w_c \nu_p^{\text{tot,slit}} + w_o \nu_p^{\text{tot,cyl}} \quad (3)$$

because the discretized pore size distribution of each shale sample contains the same pore classes that describe adsorption on these reference materials, i.e., $\nu_p^{\text{tot},j} = \sum_{k=1}^{K} \nu_{p,k}^{j}$, with $j \in$ [slit, cyl].

4.2. Model Parametrization. In addition to their shape, the selection of an appropriate number of pore classes underpins the predictive capability of the lattice DFT framework. In our previous work, an approach was presented where this selection was carried out by using the number of pore classes and the size of the pores as parameters to best fit a high-pressure CO_2 adsorption isotherm measured slightly above the critical point of the adsorbate. The rationale for the approach is that at this temperature the adsorption isotherm reveals distinct pore-size-dependent behavior, similar to subcritical physisorption analysis. While the pore size distribution derived from the subcritical isotherms has higher granularity, the volume of each pore class used in the lattice DFT model is constrained to these experimentally obtained data. The approach was applied to carbonaceous adsorbents (MC and AC)[50] and has been extended in this study to the clay sample (IL). The carbonaceous adsorbents are described by cylindrical pores with a cubic lattice packing, and both will be used here to represent the organic matter pores, to cover a sufficiently wide range of pore sizes. We note that, for some shales, the organic fraction may comprise contributions from both MC and AC. In this case, $n_{\text{cyl}}^{\text{ex}} = (1 - t)n_{\text{cyl,MC}}^{\text{ex}} + t n_{\text{cyl,AC}}^{\text{ex}}$, where t is the fraction of AC. The clay fraction of shale will be represented by IL, which can be described by slit pores with a hexagonal lattice packing.[51]

Figure 2a−c shows the lattice DFT model fits to the experimental CO_2 excess adsorption data measured on MC, AC, and IL, together with the individual contribution of each pore class (the lattice DFT "kernels"), as determined by the optimization. The pore classes selected by the optimizer and their volume fraction are presented in Figure 2d−f, alongside the continuous pore size distribution (PSD) data obtained from the analysis of the subcritical adsorption isotherms. Because the size of each bin is obtained as the cumulative contribution of pore volume between two pore classes, we do not expect the two PSDs to coincide. In fact, the aim of this task is to adequately describe the supercritical adsorption isotherm and not to match the experimental PSD.

The carbonaceous adsorbents have a fairly unimodal PSD centered around 8.4 nm (MC) and 2 nm (AC), while the data for IL indicate a multimodal distribution with important contributions from both micro- and mesopores. These features are manifested in the characteristic shape of the adsorption isotherm of each reference material, as indicated by the distinct location of the isotherm maximum, the steepness of the isotherm at low density (ρ_b < 1 mol/L), and the degree of nonlinearity of the isotherm at large bulk densities (ρ_b > 10 mol/L).[22] The values of the selected representative pore classes (number of layers, pore size, and volume fraction) are summarized in Table 2. A total of five pore classes will be used to represent each one of the two characteristic pore surfaces of shale (organic and clay). All of the remaining lattice DFT model parameters are summarized in Table S8. These will be used together with the selected pore classes to predict supercritical adsorption of CO_2 and CH_4 on four representative shale samples of varying mineralogy.

https://doi.org/10.1021/acs.energyfuels.1c03723
Energy Fuels 2022, 36, 3443−3456

Table 2. Representative Pore Classes Used for Each Surrogate Pore Surface and Their Properties[a]

adsorbent	pore geometry	pore class, k	pore size [nm], D_p or W_p	number of layers, J_k	volume fraction, $\nu_{p,k}/\nu_p^{tot}$
MC	cylindrical	1	1.2	2	0.007
		5	4.4	6	0.691
		7	11.6	15	0.302
AC	cylindrical	3	2	3	0.730
		6	8.4	11	0.270
IL	slit	2	1.6	4	0.138
		4	2	5	0.216
		8	12.4	31	0.079
		9	19.2	48	0.180
		10	36.4	91	0.387

[a]Each pore class has been assigned a value between $k = 1$ and $k = 10$ in the order of increasing pore size. J_k is the number of layers in class k.

5. RESULTS

5.1. Textural Characterization of Shale. The textural properties of all of the shales considered in this study are shown in Figure 3 and include the micropore volume (Figure 3a,b), the mesopore volume (Figure 3c,d) and the specific surface area (Figure 3e,f), as a function of TOC and clay content. The associated parameter values are reported in Table S2, together with the subcritical adsorption isotherms that have been used to extract them (Figure S1). We note that the complete distribution of pore sizes and their volume as well as the surface area of each shale sample have been obtained by combining results obtained with CO_2 (273 K) (D_p or $W_p \leq 1.5$ nm) and Ar (87 K) or N_2 (77 K) (D_p or $W_p > 1.5$ nm). In fact, as indicated in previous studies[36] and as observed for measurements on source clay minerals,[51] vapor adsorption in narrow micropores may undergo long equilibration times, which are exacerbated at cryogenic temperatures. These effects can effectively be reduced by using CO_2 as the probe molecule, because of its smaller kinetic diameter and the higher temperature of the experiment.[56] In Table S2, the micropore volumes obtained from the CO_2 measurements are systematically higher than the values estimated from the Ar (or N_2) isotherms, supporting the use of multiple probing adsorptives for textural analysis.

The textural analysis of the subcritical adsorption data allows the identification of two groups of shales: thermally mature shales (LG and ML samples, in purple) and the relatively immature shales (B samples, in blue). For each textural parameter, linear correlations obtained for each shale group are also shown in each plot (solid lines), alongside predictions based on the linear scaling of the same properties measured on the reference materials (dashed lines, pure carbon or illite, see Table S2). Two lines are shown to evaluate the scaling against the carbonaceous adsorbents, representing MC:AC ratios of 60:40 and 100:0, respectively. Notably, a positive correlation with TOC is observed for each textural parameter and for both shale groups. On the contrary, the correlations with clay content are positive only for the Bowland shales, while the data for thermally mature shales outline a negative and significant correlation in each parameter (R^2 = 0.70−0.99). The results also indicate that there is a fairly good agreement between values of the micropore volume and the specific surface area predicted from the perfect linear scaling of the carbonaceous adsorbent properties and the measured counterparts. In particular, the prediction of these properties for the Bowland shale samples requires a lower AC:MC ratio, as compared to the more thermally mature shales. A similar good agreement is observed for Bowland shales between textural property predictions based on the linear scaling of the illite source clay mineral and the measured values. These trends and the linear form of these correlations also agree with the literature on various other shales.[17,57]

In Figure 3g,h the maximum excess amount adsorbed measured with CO_2 and CH_4 on four shale samples (LG4, ML, B6, and B8) is plotted as a function of TOC (Figure 3g) and clay content (Figure 3h). These data have been obtained at a temperature of 40 °C and at a pressure of approximately 8 MPa (CO_2) and 10 MPa (CH_4). For both adsorbates, we observe a positive and significant correlation (R^2 = 0.91) with TOC. On the contrary, we do not find any correlation with the clay content. This result indicates that the contribution of clays to gas adsorption in shale is more complex than that of the organic content. One indication confirming this increased complexity was already given above, where a change in the sign of the correlation between textural properties and clay content was observed with increasing thermal maturity of the shale (Figure 3b,d,f). When plotted against TOC, we also observe that for both gases the predictions from the linear scaling of values measured on mesoporous carbon (MC) underestimate adsorption relative to direct measurements on shales. This further implies that particular care should be taken in selecting the reference carbon materials in the development of the "kernels" to be used in the hybrid lattice DFT adsorption model; in this study, we consider a synthetic mixture of AC and MC to cover a broader range of pore sizes, this being particularly important for the more mature shales (high TOC, see next section). Moreover, we expect clays to contribute to gas uptake, too—playing an increasing role with a decrease in thermal maturity (Longmaxi > Marcellus > Bowland shales) and/or for shales with high clay content (>40 wt %). In fact, as discussed above, the adsorption process is expected to be controlled by the extent of microporosity and the available surface area, these being textural properties that show a positive and significant correlation with clay content in shale (Figure 3b,f).

5.2. Supercritical CO_2 and CH_4 Adsorption on Shale. The complete set of unary CO_2 and CH_4 excess adsorption isotherms measured at 40 °C on the LG4, ML, B6, and B8 shales is shown in Figure 4 as a function of the bulk density, ρ_b. The tabulated results are included in Tables S4−S7. For all shales, the shape of the CO_2 excess adsorption isotherms closely reproduces the one observed for the reference mesoporous materials (MC and IL), including the location of the maximum at $\rho_b \approx 5-7$ mol/L. The excess adsorption isotherm shows an initial steep increase with bulk fluid density, followed by a clear bending (knickpoint) characteristic of mesoporous materials,[22] before decreasing nonlinearly with a further increase in bulk fluid density and approaching $n^{ex} \approx 0$ at very high densities ($\rho_b > 20$ mol/L). At these conditions, the material's pore space is completely filled with a single fluid phase (bulk and adsorbed phase cannot be distinguished). The CH_4 isotherms indicate that this point is not reached with any of the shale samples, and their maxima are reached at slightly smaller bulk densities, as compared to CO_2. In fact, at the highest pressure attained in the measurements (about 30 MPa), the bulk density of CH_4 is much lower compared to

https://doi.org/10.1021/acs.energyfuels.1c03723
Energy Fuels 2022, 36, 3443−3456

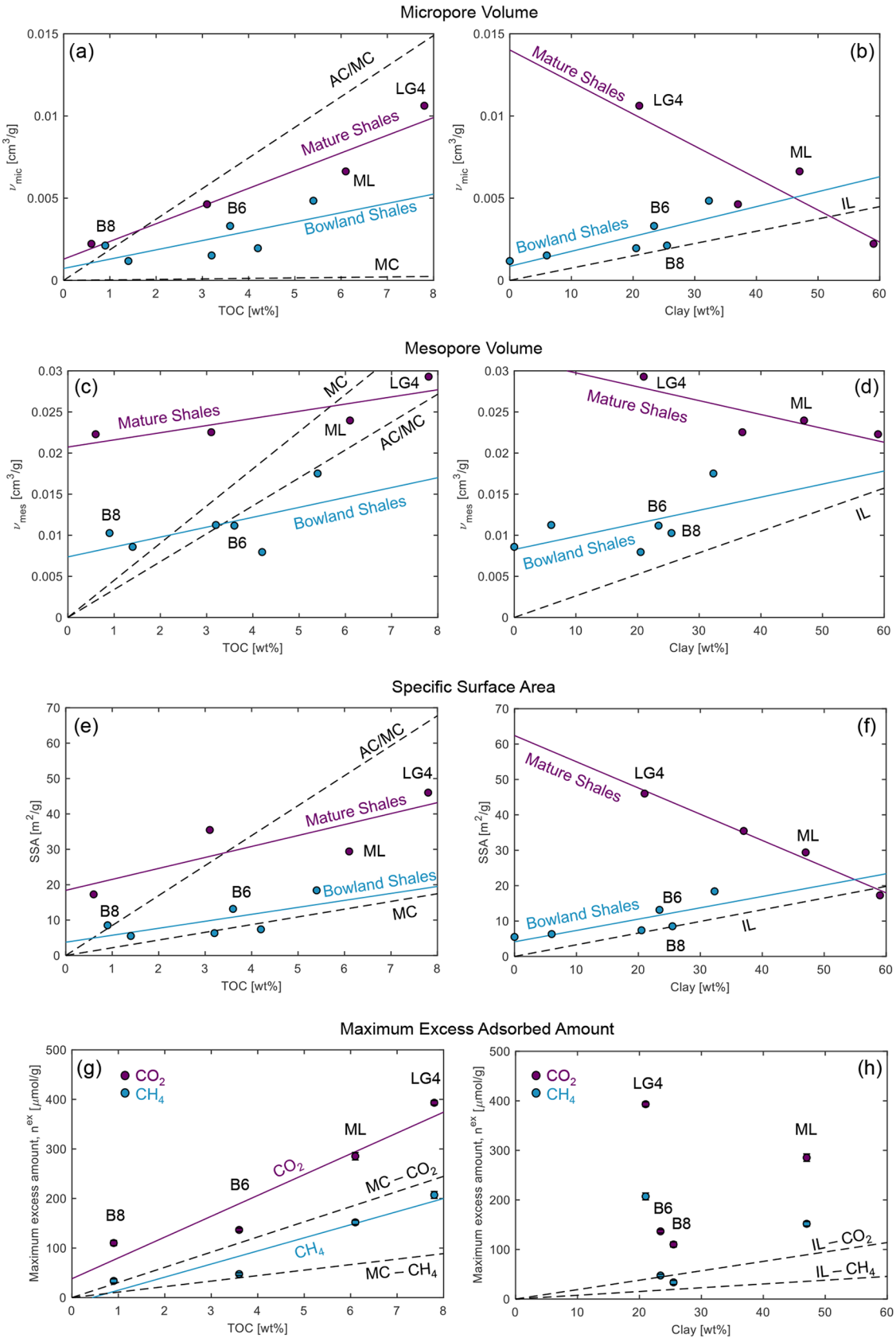


Figure 3. Micropore volume (a, b), mesopore volume (c, d), specific surface area (e, f), and maximum excess adsorbed amount at 40 °C (g, h) of the shale samples considered in this study as a function of TOC or clay content. Points show the properties derived from experimental measurements, and solid lines denote lines of best fit. Dashed lines denote the scaled textural properties of MC/AC (60:40 ratio) or pure MC or IL.

https://doi.org/10.1021/acs.energyfuels.1c03723
Energy Fuels 2022, 36, 3443−3456

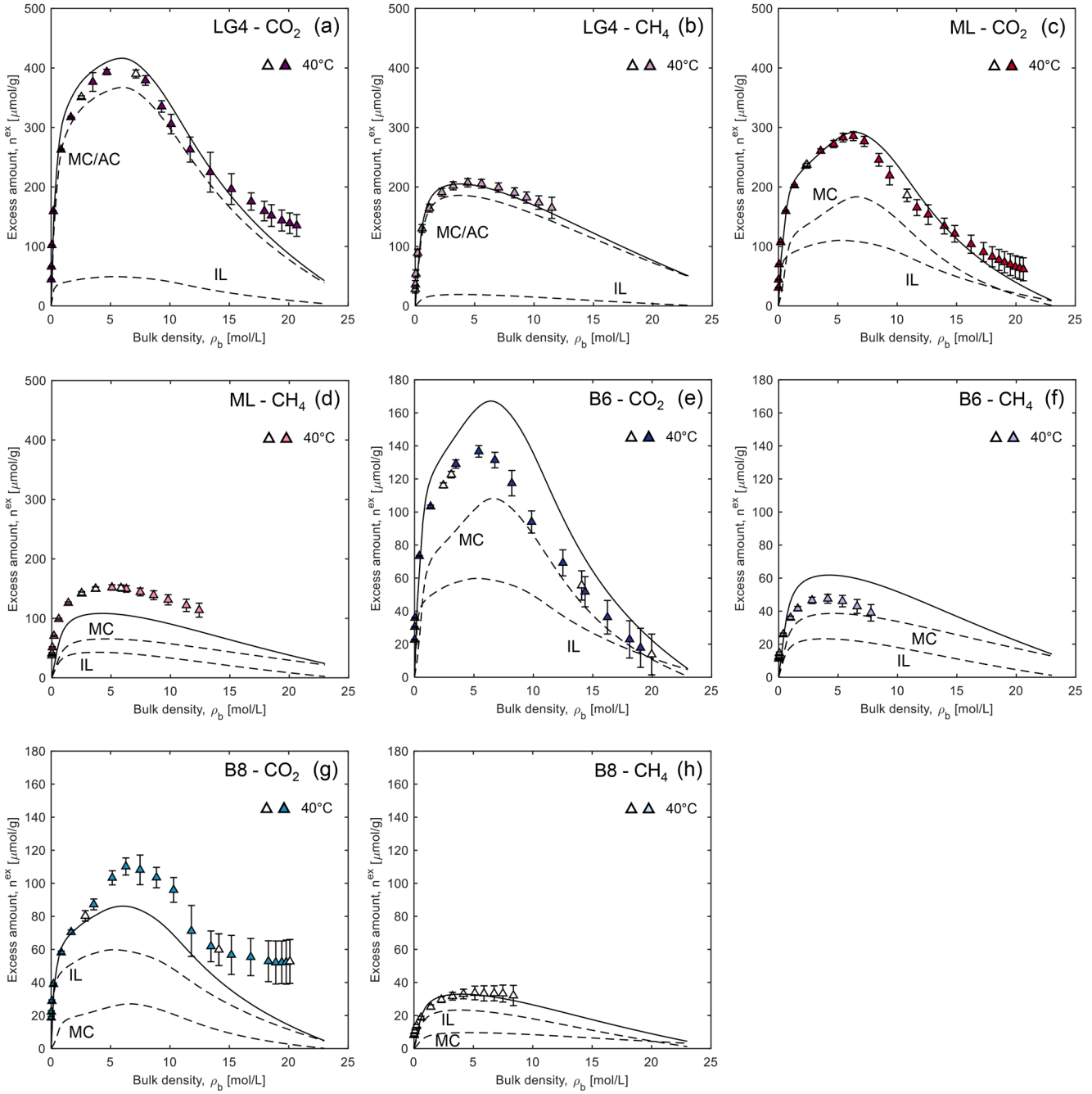


Figure 4. Excess CO_2 and CH_4 adsorption isotherms for (a, b) LG4, (c, d) ML, (e, f) B6 and (g, h) B8 at 40 °C (empty symbols denote data taken in adsorption mode, and filled symbols represent data taken in desorption mode) and synthetic isotherms (solid lines) comprising summed scaled MC, AC, and illite lattice DFT modeled isotherms at the same temperature. The scaling factors used for the modeled isotherms are based on each shale's TOC and clay content. Dashed lines show the individual contribution from MC, AC, and IL.

CO_2, as the experimental temperature is farther from the adsorbate critical temperature.

When comparing the adsorption isotherms measured on these four shales samples, it becomes apparent that the more organic-rich and thermally mature shales (LG4 and ML) adsorb approximately 2−3 times the amount of gas adsorbed on the Bowland shales. For CO_2, the maximum excess amount adsorbed decreases in the following order: LG4 (~400 μmol/g) > ML (~290 μmol/g) > B6 (~140 μmol/g) > B8 (~110 μmol/g). The same order is observed for CH_4, namely, LG4 (~210 μmol/g) > ML (~150 μmol/g) > B6 (~50 μmol/g) > B8 (~35 μmol/g). For both CO_2 and CH_4, the ratio of the maximum excess adsorption measured on LG4 and ML (~1.4) approximates the ratio of TOC of the two shales (~1.3). Within the Bowland shales, a similar ratio in the adsorbed amounts (B6:B8) is observed, albeit the TOC ratio is substantially higher (~4). This result is notable because B6 and B8 have a similar amount of clay minerals (~25 wt %), highlighting once more the important, yet complex, contribution of clay minerals to gas uptake in shale. CO_2 adsorbs more than CH_4 on all shales. For the two Bowland shale samples, the CO_2/CH_4 ratio of the maximum excess amount adsorbed is

https://doi.org/10.1021/acs.energyfuels.1c03723
Energy Fuels 2022, 36, 3443−3456

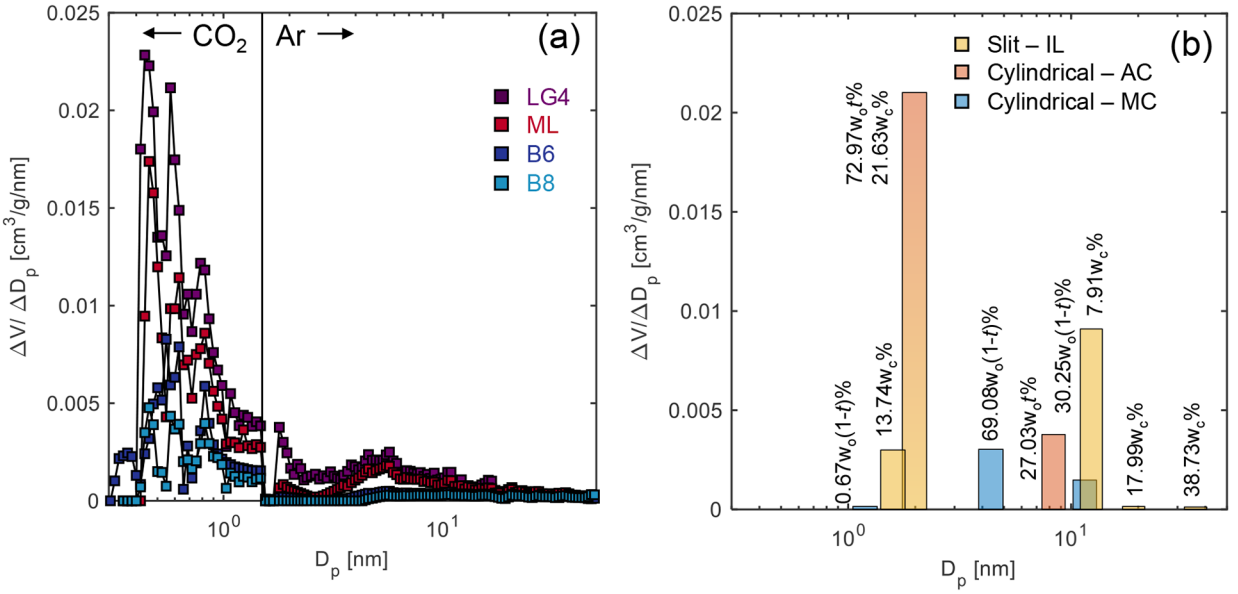


Figure 5. (a) Pore size distribution (up to 50 nm) obtained from the Ar (87 K) and CO_2 (273 K) adsorption data using the NLDFT and GCMC models for all shales. (b) Discretized PSD representing the PSD of the shales. The bars represent a combination of the discretized PSD obtained from the lattice DFT model applied to MC (blue bars), AC (orange bars), and IL (yellow bars). The selected pore sizes correspond exactly to the pore sizes from Figure 2. The volume assigned to each bar is also based on the same idealized adsorbents but is scaled using three scaling factors: w_0, representing the TOC fraction in the shale; w_c, indicating the clay content of the shale; and t, which denotes the fraction of AC (as a representative of the elevated interaction with the organic material) to be used in the discretized PSD. The dual-colored bar at 2 nm includes contributions from both AC and IL. The example PSD shown is for LG4, where w_0 = 0.078, w_c = 0.21, and t = 0.25.

approximately 3, a value that is larger than the CO_2/CH_4 ratio of 2 obtained for the more thermally mature shales (LG4 and ML).

Figure 4 shows alongside the experimental data the model-predicted excess adsorption isotherms (solid lines). These have been obtained by the weighted sum of the lattice DFT isotherms of illite (IL), as the surrogate for clay pore surfaces in shale, and of mesoporous carbon (MC) and/or activated carbon (AC), as the surrogates for organic pore surfaces in shale. This analysis is predictive, because it uses only the shale composition (clay content and TOC, see Table 1) to individually scale these reference isotherms. To our surprise, there is a very good agreement between the experiments and the model predictions, considering that the shales show varied composition in terms of TOC and clay content and feature distinct adsorption strength for both CO_2 and CH_4. We note that the carbon surface in LG4 is represented by an AC:MC ratio of 1:4, which was required to prevent the underestimation of the excess amount adsorbed observed when using MC as the sole surrogate organic-rich surface. AC represents a more microporous carbon, which also shows a higher surface interaction energy.[50] Here, we have interpreted these properties as being features of a thermally mature shale.

In Figure 4 are also shown the individual contributions of the scaled pure carbon(s) and illite isotherms. For LG4, the carbon surface clearly dominates the overall adsorption behavior for both CO_2 and CH_4. For ML and B6, the contribution of the clays to the adsorption of both adsorbates has increased, albeit it remains smaller than the one imparted by the carbon surface. However, at very low bulk densities (ρ_b < 1 mol/L), the clays control by and large the adsorption process, as indicated by the crossing of the MC and IL isotherms for CO_2. For the organic-lean B8 sample, the situation is reversed, with IL contributing the most to the adsorption isotherm for both CO_2 and CH_4. These observations confirm by and large the trends discussed in the previous section (Textural Characterization of Shale), providing an important verification of the proposed "kernels" to predict supercritical adsorption in shale. The isotherm plots shown in Figure 4 clearly demonstrate the benefits of explicitly accounting for distinct carbon and clay surfaces in the hybrid lattice DFT model. In fact, AC, MC, and IL feature distinct isotherm shapes, and only their combination leads to an accurate representation of the shale isotherm. As such, the measurements with CO_2 represent a key element in the application of the approach proposed here, because of the manifestation of pore-dependent adsorption behaviors at near-critical conditions.

6. DISCUSSION

The benefit of a model-predictive approach to supercritical gas adsorption on morphologically and chemically heterogeneous adsorbents, such as shales, cannot be underestimated, as the high-pressure adsorption experiments are very involved and time-consuming. The results presented in this study show that micro-/mesoporous carbons and source clays can be used as surrogates for the organic and clay surfaces of shale. Isotherms measured on these materials can be used as "kernels" and combined in a proportion that reproduces the shale's clay and TOC content to build a composite adsorption isotherm. In this study, the analysis was limited to adsorption isotherms measured at 40 °C, but the model can be readily used at other temperatures, because temperature is represented explicitly in the Ono-Kondo lattice equations. Moreover, while both lattice adsorbate−adsorbate and adsorbate−adsorbent interaction parameters do not depend on temperature, the so-called saturation factor in eq 1 does. We have previously shown that this parameter has a linear relationship

https://doi.org/10.1021/acs.energyfuels.1c03723
Energy Fuels 2022, 36, 3443−3456

with the reciprocal temperature for both clays and carbons,[50,51] suggesting that the approach presented in this study may also have predictive validity. In the following, we extend this analysis to obtain a representative pore size distribution for shales, purely based on the surrogate surfaces used in the prior section. For each shale play considered in this study, we also carry out an assessment of the expected gas-in-place by using the experimental and modeling results.

6.1. Representative Pore Size Distribution for Shales. Figure 5a shows the PSDs of the four shale samples that have been used in the supercritical CO_2 and CH_4 adsorption study presented in the previous section. These data have been derived from the subcritical Ar and CO_2 isotherms and feature a diverse range of pore sizes. It can be seen that the four shale samples possess a similar PSD, featuring two distinct peaks at approximately 0.6−0.8 nm (micropores) and 4−6 nm (mesopores), respectively. The distributions are also characterized by a distinctive shoulder at 1−2 nm. Above 50 nm (not shown in the figure), the PSD is effectively identical for the four materials. In more quantitative terms, there is an obvious trend in the peaks' heights associated with micro- and mesopores in the order LG4 > ML > B6 > B8. Notably, this is also the order of decreasing pore volume (in both micro- and mesopore classes) and of decreasing TOC in each shale. It is worth noting that these PSDs have been obtained by applying pore-scale adsorption model kernels, which have been developed for synthetic material classes and pore geometries (i.e., carbon slit pores *or* silica cylindrical pores, but not their combination). Their application to shales might result in textural properties that deviate from physical reality, because this conceptualization may oversimplify the surface properties of shale. Methods are needed that evaluate and possibly validate the reliability of these predictions, as discussed in the following.

The good agreement between the experimental supercritical adsorption isotherms presented in Section 5.2 and predictions by the hybrid lattice DFT model suggests that the discretized PSD used by the latter provides for a good representation of the shale's PSD. This discretized PSD is shown in Figure 5b and includes cylindrical pores of diameter D_p = [1.2, 2, 4.4, 8.4, 11.6] nm (blue and orange bars, representing pore classes in MC and AC) and slit pores of width W_p = [1.6, 2, 12.4, 19.2, 36.4] nm (yellow bars, representing pore classes in IL). The brown bar at 2 nm signifies the representation of this pore class by both slit (IL) and cylindrical (AC) pores. This PSD can be considered as universal, but the contribution of each pore class will change depending on the shale's thermal maturity, TOC, and clay content, as indicated by the label adjacent to each bar. The example shown in Figure 5b represents sample LG4. Three scaling factors have been used: (i) w_0, the TOC (wt %) in the shale; (ii) w_c, the clay content (wt %) in the shale; and (iii) t, the fraction of w_0 that is accounted for by AC, as a proxy for a thermally mature shale ($1 - t$ represents, therefore, the MC fraction). In general, it can be seen that the discretized PSD does capture the dominant features (peaks) present in the data obtained from the interpretation of the subcritical adsorption measurements. We note the systematic shift toward larger pore diameters of the PSD used by the lattice DFT model, particularly for the micropores ($D_p \leq 2$ nm). This is due to the fact that, in the lattice model, pore sizes can only be exact integers of the assumed molecule size (d = 0.4 nm), and that the smallest pore size that can be considered is $L = 2d$.

Table 3 provides a comparison between the total pore volume predicted by the method described above (eq 3) and the one extracted from the subcritical adsorption experiments (Table S2) for the four shale samples. Overall, there is a good agreement between the two sets of data. Notably, the hybrid lattice DFT approach preserves the trend observed experimentally, where the total pore volume decreases in the order LG4 > ML > B6 > B8. This result is noteworthy, considering that the shale samples differ substantially in their TOC (1−8 wt %) and total pore volume (0.02−0.05 cm^3/g). As such, this discretized PSD may prove to be useful for the analysis of any shale, even outside this study.

Table 3. Total Pore Volume Estimated by Physisorption Measurements and Predicted by the Hybrid Lattice DFT Model for Each Shale

shale	experimental [cm^3/g]	predicted [cm^3/g]
LG4	0.050	0.049
ML	0.042	0.050
B6	0.020	0.028
B8	0.020	0.016

6.2. Gas-in-Place. The gas-in-place (GIP) serves as a useful means to quantitatively asses the economic potential of a shale play. It directly quantifies the amount of CH_4 that can be recovered or the amount of CO_2 that can be stored in a shale reservoir as a function of pressure. The ability to estimate this measure directly from experimental excess adsorption data or through a suitable adsorption model would prove beneficial to explore strategies for an optimized reservoir exploitation.[9] The GIP [m^3_{STP}/m^3] can be calculated using the following expression:

$$\mathrm{GIP} = G_t = \frac{1}{\rho_{sc}}(\rho_b \phi + n^{ex}(1 - \phi)\rho_{sk}) \tag{4}$$

where ρ_{sc} is the gas density at standard conditions (ρ_{sc} = 44.135 mol/m^3_{STP} for CH_4 and ρ_{sc} = 44.326 mol/m^3 for CO_2[58]), ϕ is the reservoir porosity, ρ_b [mol/m^3] is the gas bulk density, n^{ex} [mol/kg] is the excess amount adsorbed, and ρ_{sk} [kg/m^3] is the skeletal density of the shale. The first term in eq 4 represents the volumetric free gas in the reservoir, and the second term describes adsorption.[9] Both terms depend on the bulk density of the gas, albeit in different ways. Material balance calculations for primary recovery use a graphical approach, where the volume of gas produced (G_p) is plotted as a function of P/Z ($= \rho_b RT$, where R and T are the universal gas constant and temperature, respectively, and Z is the gas compressibility). Mathematically

$$G_p = G_{t,0} - \mathrm{GIP} \tag{5}$$

where $G_{t,0}$ is the original GIP (OGIP), obtained at $P/Z = 0$. In Figure 6a are shown the $G_p - P/Z$ curves for the four shales considered in this study. For these calculations, we have assumed a reservoir porosity, ϕ = 5%, while the skeletal density for each shale, ρ_{sk} = 2.6−2.7 g/cm^3, is based on the helium measurement (the exact values can be found in Table S3). The symbols refer to results obtained by using the experimental adsorption data described in Section 5.2 (T = 40 °C), which have been restricted here to below 200 bar to facilitate comparisons among the shales. The dashed lines solely represent the volumetric free gas component in eq 4, while the solid lines are obtained upon describing the adsorption

https://doi.org/10.1021/acs.energyfuels.1c03723
Energy Fuels 2022, 36, 3443−3456

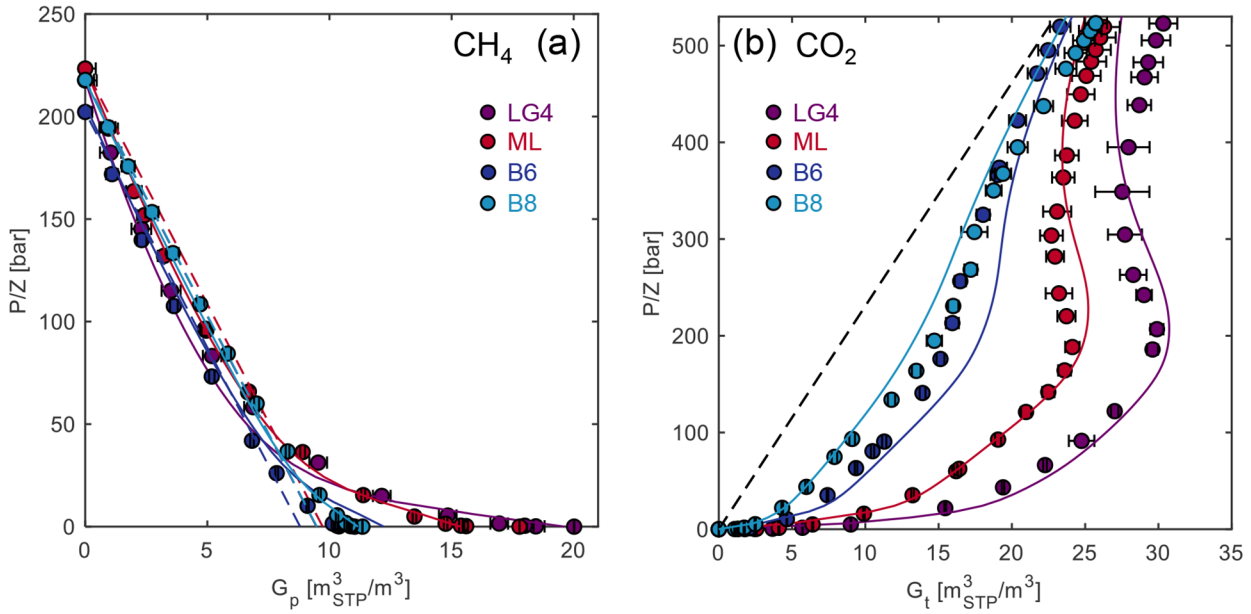


Figure 6. (a) Volume of CH_4 produced (G_p) as a function of P/Z at 40 °C for the four shale samples considered in this study. The assumed initial reservoir pressure is 186 bar (LG4, B8), 191 bar (ML), and 173 bar (B6). (b) CO_2 storage potential, G_t, as a function of P/Z for each shale at 40 °C for an injection pressure up to 260 bar. Dashed lines represent the volumetric free gas, and the symbols denote data calculated from the excess adsorption measurements. Solid lines represent G_p (CH_4) or G_t (CO_2) calculated from the modeled lattice DFT adsorption isotherms.

term by the hybrid lattice DFT model results discussed previously. Again, the lattice DFT model describes the experimental production curves with satisfactory accuracy.

The shales' OGIP decreases in the following order: LG4 (20.0 m^3_{STP}/m^3) > ML (17.8 m^3_{STP}/m^3) > B8 (11.3 m^3_{STP}/m^3) > B6 (11.0 m^3_{STP}/m^3)—reproducing the same trend observed for the strength of adsorption (Figure 3g). For a volumetric gas reservoir (no adsorption, dashed lines), the G_p–P/Z curves are straight lines, and the OGIP reduces substantially. For the organic-rich shales (LG4, ML), this reduction can be as high as 50%. We also note that the largest contribution of adsorption to gas production is observed for P/Z values smaller than approximately 50 bar; above this threshold, gas production may actually be less than estimates obtained by assuming a volumetric gas reservoir (the solid lines are below the dashed lines). The reason for this is that at such elevated pressures simple gas compression leads to greater storage than adsorption alone.[9]

Figure 6b shows the GIP curves for a situation where CO_2 is injected into a depleted reservoir. By assuming a maximum pressure of 260 bar, the following estimates for the storage potential of each shale are obtained: 30.3 m^3_{STP}/m^3 (LG4), 26.3 m^3_{STP}/m^3 (ML), 23.3 m^3_{STP}/m^3 (B6), and 25.7 m^3_{STP}/m^3 (B8). These values are substantially larger than those obtained for CH_4, because CO_2 has a larger density and adsorbs more strongly than CH_4 (at equivalent P/Z). Again, the lattice DFT model (solid lines) describes the experimental storage curves (symbols) with satisfactory accuracy. Adsorption contributes to gas storage from the outset ($P/Z > 0$), with the curves deviating substantially from the case of a volumetric reservoir with the same porosity (dashed line). With increasing pressure ($P/Z > 200$ bar), the densification of bulk CO_2 becomes more dominant, and the curves approach the behavior of the volumetric reservoir ($n^{ex} \approx 0$). The analysis presented in this section demonstrates that the use of the hybrid lattice DFT model can be extended to the evaluation of shale plays, by producing estimates of GIP and storage potential. In this context, the approach introduced in this study that uses surrogate surfaces may prove to be a practical and efficient method for a first appraisal of a particular shale's economic potential.

7. CONCLUSION

We have presented a hybrid pore-scale model to describe supercritical adsorption of CO_2 and CH_4 in shale. The model is based on the lattice density functional theory (DFT) and incorporates the distinct pore morphologies (slit or cylindrical pores) and surface chemistries (carbon or clay) that exist within shale. The shales studied in this paper come from the Bowland (UK), Marcellus (USA), and Longmaxi (China) formations. The surrogate surfaces used (mesoporous carbon/activated carbon and illite) are representative of the total organic content and the total clay content in shale, respectively. The model is parametrized by calibration against these reference materials, and its application to describe experimental shale adsorption data is purely predictive, solely utilizing the shale's composition. This proposed workflow is particularly advantageous from a practical perspective, as it minimizes the need for time-consuming and challenging high-pressure adsorption experiments. The textural characterization undertaken as well as the high-pressure adsorption experiments firmly suggest a strong dependency of adsorption capacity on the TOC. Clays do also participate in the gas adsorption process, particularly at elevated clay content, but their contribution is more difficult to unravel. Through the model, we have identified a representative discretized pore size distribution that includes both micro- and mesopores. Again, the exact contribution of each pore class depends on the shale's composition, meaning that it can be readily applied to any other shale. The ability to identify characteristic pore-scale properties, including size, morphology, and surface chemistry, provides useful information for future in-depth molecular

https://doi.org/10.1021/acs.energyfuels.1c03723
Energy Fuels 2022, 36, 3443−3456

simulation studies. In this study, the use of the hybrid lattice DFT model has been extended to generate estimates of gas-in-place and gas storage potential. As such, the approach introduced in this study that uses surrogate surfaces may prove to be a practical and efficient method for a first appraisal of a particular shale's economic potential.

■ ASSOCIATED CONTENT

Supporting Information

The Supporting Information is available free of charge at https://pubs.acs.org/doi/10.1021/acs.energyfuels.1c03723.

Tabulated shale adsorption data, textural characterization, shale mineralogy, and lattice DFT model parameters (PDF)

■ AUTHOR INFORMATION

Corresponding Author

Ronny Pini − *Department of Chemical Engineering, Imperial College London, London SW7 2AZ, United Kingdom;* orcid.org/0000-0002-9443-3573; Email: r.pini@imperial.ac.uk

Authors

Humera Ansari − *Department of Chemical Engineering, Imperial College London, London SW7 2AZ, United Kingdom*

Shuwei Gong − *Department of Chemical Engineering, Imperial College London, London SW7 2AZ, United Kingdom*

JP Martin Trusler − *Department of Chemical Engineering, Imperial College London, London SW7 2AZ, United Kingdom;* orcid.org/0000-0002-6403-2488

Geoffrey Maitland − *Department of Chemical Engineering, Imperial College London, London SW7 2AZ, United Kingdom*

Complete contact information is available at: https://pubs.acs.org/10.1021/acs.energyfuels.1c03723

Notes

The authors declare no competing financial interest.

■ ACKNOWLEDGMENTS

H.A. acknowledges the Marit Mohn Scholarship at Imperial College London. We are grateful to the funding provided by the Commonwealth Scientific and Industrial Research Organisation (CSIRO). We also thank Jabraan Ahmed from University College London for measuring the composition of the Bowland shales.

■ NOMENCLATURE

Symbols

c^{sat} = saturation factor
d = diameter of a lattice site
D_p = diameter of a cylindrical pore
ε_{ff} = adsorbate−adsorbate interaction energy
ε_{sf} = adsorbate−adsorbent interaction energy
G_t = gas-in-place
G_p = cumulative amount of gas produced
$G_{t,0}$ = OGIP
J_k = number of layers in pore class k
K = number of pore classes
n^{ex} = excess adsorbed amount
n^{ex}_{cyl} = excess amount adsorbed for cylindrical pores
n^{ex}_{slit} = excess amount adsorbed for slit pores
ϕ = porosity
P = pressure
P_c = critical pressure
ρ_b = bulk fluid density
ρ_c = critical density
ρ_j = density in layer j
ρ_{max} = maximum lattice density
ρ_{sc} = density of the fluid at standard conditions
ρ_{sk} = skeletal density
R = universal gas constant
t = fraction of AC
T = temperature
T_c = critical temperature
ν_{mic} = micropore volume
ν_{mes} = mesopore volume
ν_{tot} = total pore volume
$\nu_{p,k}$ = pore volume of pore class k
w_c = weight fraction of clay
w_0 = weight fraction of organic matter
W_p = diameter of a slit pore
Z = fluid compressibility

Acronyms

AC = activated carbon
B_ = Bowland shale
CM = clay minerals
DFT = density functional theory
GIP = gas-in-place
GCMC = Grand Canonical Monte Carlo
IL = illite
LDFT = lattice density functional theory
LG = Longmaxi shale
MC = mesoporous carbon
ML = Marcellus shale
MSB = magnetic suspension balance
NLDFT = nonlocal density functional theory
OGIP = original gas-in-place
OM = organic matter
PSD = pore size distribution
SSA = specific surface area
TOC = total organic carbon

■ REFERENCES

(1) *World Energy Outlook 2019*; Report for IEA, 2019.

(2) Godec, M.; Koperna, G.; Petrusak, R.; Oudinot, A. Potential for enhanced gas recovery and CO_2 storage in the Marcellus Shale in the Eastern United States. *International Journal of Coal Geology* **2013**, *118*, 95−104.

(3) Tao, Z.; Clarens, A. Estimating the Carbon Sequestration Capacity of Shale Formations Using Methane Production Rates. *Environ. Sci. Technol.* **2013**, *47*, 11318−11325.

(4) Ma, L.; Fauchille, A.-L.; Ansari, H.; Chandler, M.; Ashby, P.; Taylor, K.; Pini, R.; Lee, P. D. Linking multi-scale 3D microstructure to potential enhanced natural gas recovery and subsurface CO_2 storage for Bowland shale, UK. *Energy Environ. Sci.* **2021**, *14*, 4481−4498.

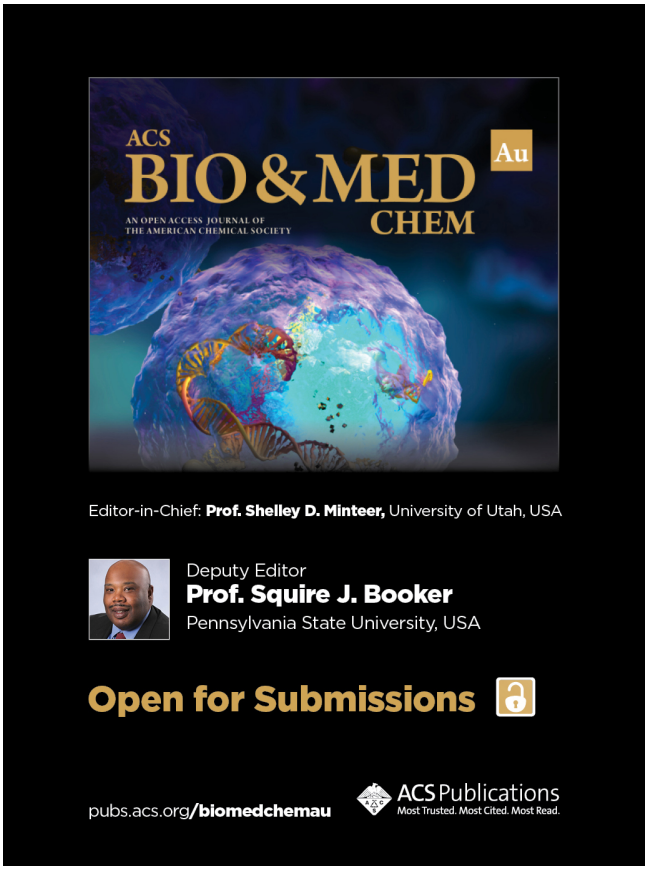
(5) Pini, R. Assessing the Adsorption Properties of Mudrocks for CO_2 Sequestration. *Energy Procedia* **2014**, *63*, 5556−5561.

(6) Gasparik, M.; et al. First international inter-laboratory comparison of high-pressure CH_4, CO_2 and C_2H_6 sorption isotherms on carbonaceous shales. *International Journal of Coal Geology* **2014**, *132*, 131−146.

(7) Charoensuppanimit, P.; Mohammad, S. A.; Gasem, K. A. M. Measurements and Modeling of Gas Adsorption on Shales. *Energy Fuels* **2016**, *30*, 2309−2319.
(8) Xu, R.; Zeng, K.; Zhang, C.; Jiang, P. Assessing the feasibility and CO_2 storage capacity of CO_2 enhanced shale gas recovery using Triple-Porosity reservoir model. *Applied Thermal Engineering* **2017**, *115*, 1306−1314.
(9) Ansari, H.; Rietmann, E.; Joss, L.; Trusler, J. P. M.; Maitland, G.; Pini, R. A shortcut pressure swing adsorption analogue model to estimate Gas-in-Place and CO_2 storage potential of gas shales. *Fuel* **2021**, *301*, 121014.
(10) Ambrose, R. J.; Hartman, R. C.; Diaz-Campos, M.; Akkutlu, I. Y.; Sondergeld, C. H. Shale Gas-in-Place Calculations Part I: New Pore-Scale Considerations. *SPE Journal* **2012**, *17*, 219−229.
(11) Kang, S. M.; Fathi, E.; Ambrose, R. J.; Akkutlu, I. Y.; Sigal, R. F. Carbon Dioxide Storage Capacity of Organic-Rich Shales. *SPE Journal* **2011**, *16*, 842.
(12) Chalmers, G. R.; Bustin, R. M.; Power, I. M. Characterization of gas shale pore systems by porosimetry, pycnometry, surface area, and field emission scanning electron microscopy/transmission electron microscopy image analyses: Examples from the Barnett, Woodford, Haynesville, Marcellus, and Doig units. *AAPG Bulletin* **2012**, *96*, 1099−1119.
(13) Wu, C.; Tuo, J.; Zhang, L.; Zhang, M.; Li, J.; Liu, Y.; Qian, Y. Pore characteristics differences between clay-rich and clay-poor shales of the Lower Cambrian Niutitang Formation in the Northern Guizhou area, and insights into shale gas storage mechanisms. *International Journal of Coal Geology* **2017**, *178*, 13−25.
(14) Sposito, G.; Skipper, N. T.; Sutton, R.; Park, S.; Soper, A. K.; Greathouse, J. A. Surface geochemistry of the clay minerals. *Proc. Natl. Acad. Sci. U. S. A.* **1999**, *96*, 3358−3364.
(15) Loucks, R. G.; Reed, R. M.; Ruppel, S. C.; Jarvie, D. M. Morphology, Genesis, and Distribution of Nanometer-Scale Pores in Siliceous Mudstones of the Mississippian Barnett Shale. *Journal of Sedimentary Research* **2009**, *79*, 848−861.
(16) Ma, L.; Taylor, K. G.; Lee, P. D.; Dobson, K. J.; Dowey, P. J.; Courtois, L. Novel 3D centimetre-to nano-scale quantification of an organic-rich mudstone: The Carboniferous Bowland Shale, Northern England. *Marine and Petroleum Geology* **2016**, *72*, 193−205.
(17) Ross, D. J. K.; Bustin, R. M. The importance of shale composition and pore structure upon gas storage potential of shale gas reservoirs. *Marine and Petroleum Geology* **2009**, *26*, 916−927.
(18) Tang, X.; Ripepi, N.; Stadie, N. P.; Yu, L.; Hall, M. R. A dual-site Langmuir equation for accurate estimation of high pressure deep shale gas resources. *Fuel* **2016**, *185*, 10−17.
(19) Ye, Z.; Chen, D.; Pan, Z.; Zhang, G.; Xia, Y.; Ding, X. An improved Langmuir model for evaluating methane adsorption capacity in shale under various pressures and temperatures. *Journal of Natural Gas Science and Engineering* **2016**, *31*, 658−680.
(20) Yu, W.; Sepehrnoori, K.; Patzek, T. W. Modeling Gas Adsorption in Marcellus Shale With Langmuir and BET Isotherms. *SPE Journal* **2016**, *21*, 589−600.
(21) Tang, X.; Ripepi, N.; Luxbacher, K.; Pitcher, E. Adsorption Models for Methane in Shales: Review, Comparison, and Application. *Energy Fuels* **2017**, *31*, 10787−10801.
(22) Pini, R.; Ansari, H.; Hwang, J. Measurement and interpretation of unary supercritical gas adsorption isotherms in micro-mesoporous solids. *Adsorption* **2021**, *27*, 659−671.
(23) Yang, N.; Liu, S.; Yang, X. Molecular simulation of preferential adsorption of CO_2 over CH_4 in Na-montmorillonite clay material. *Appl. Surf. Sci.* **2015**, *356*, 1262−1271.
(24) Liu, Y.; Zhu, Y.; Li, W.; Xiang, J.; Wang, Y.; Li, J.; Zeng, F. Molecular simulation of methane adsorption in shale based on grand canonical Monte Carlo method and pore size distribution. *Journal of Natural Gas Science and Engineering* **2016**, *30*, 119−126.
(25) Wang, T.; Tian, S.; Li, G.; Sheng, M. Selective adsorption of supercritical carbon dioxide and methane binary mixture in shale kerogen nanopores. *Journal of Natural Gas Science and Engineering* **2018**, *50*, 181−188.
(26) Liu, Y.; Li, H. A.; Tian, Y.; Jin, Z.; Deng, H. Determination of the absolute adsorption/desorption isotherms of CH_4 and n-C_4H_10 on shale from a nano-scale perspective. *Fuel* **2018**, *218*, 67−77.
(27) Liu, J.; Xi, S.; Chapman, W. G. Competitive Sorption of CO_2 with Gas Mixtures in Nanoporous Shale for Enhanced Gas Recovery from Density Functional Theory. *Langmuir* **2019**, *35*, 8144−8158.
(28) Xu, R.; Prodanovi, M.; Landry, C. J. Study of subcritical and supercritical gas adsorption behavior in different nanopore systems in shale using lattice Boltzmann method. *International Journal of Coal Geology* **2019**, *212*, 103263.
(29) Zhang, T.; Sun, S. A coupled Lattice Boltzmann approach to simulate gas flow and transport in shale reservoirs with dynamic sorption. *Fuel* **2019**, *246*, 196−203.
(30) Jiang, W.; Lin, M. Molecular dynamics investigation of conversion methods for excess adsorption amount of shale gas. *Journal of Natural Gas Science and Engineering* **2018**, *49*, 241−249.
(31) Foroozesh, J.; Abdalla, A. I. M.; Zhang, Z. Pore Network Modeling of Shale Gas Reservoirs: Gas Desorption and Slip Flow Effects. *Transport in Porous Media* **2019**, *126*, 633−653.
(32) Collell, J.; Galliero, G.; Gouth, F.; Montel, F.; Pujol, M.; Ungerer, P.; Yiannourakou, M. Molecular simulation and modelisation of methane/ethane mixtures adsorption onto a microporous molecular model of kerogen under typical reservoir conditions. *Microporous Mesoporous Mater.* **2014**, *197*, 194−203.
(33) Cristancho-Albarracin, D.; Akkutlu, I. Y.; Criscenti, L. J.; Wang, Y. Shale gas storage in kerogen nanopores with surface heterogeneities. *Appl. Geochem.* **2017**, *84*, 1−10.
(34) Xu, R.; Prodanovi, M. Effect of pore geometry on nitrogen sorption isotherms interpretation: A pore network modeling study. *Fuel* **2018**, *225*, 243−255.
(35) Xu, R.; Prodanovi, M.; Landry, C. Pore-Scale Study of Water Adsorption and Subsequent Methane Transport in Clay in the Presence of Wettability Heterogeneity. *Water Resour. Res.* **2020**, *56*, No. e2020WR027568.
(36) Wang, H.; Qu, Z.; Yin, Y.; Bai, J.; Yu, B. Review of Molecular Simulation Method for Gas Adsorption/desorption and Diffusion in Shale Matrix. *Journal of Thermal Science* **2019**, *28*, 1−16.
(37) Aranovich, G.; Donohue, M. Analysis of Adsorption Isotherms: Lattice Theory Predictions, Classification of Isotherms for GasSolid Equilibria, and Similarities in Gas and Liquid Adsorption Behavior. *J. Colloid Interface Sci.* **1998**, *200*, 273−290.
(38) Hocker, T.; Rajendran, A.; Mazzotti, M. Measuring and Modeling Supercritical Adsorption in Porous Solids. Carbon Dioxide on 13X Zeolite and on Silica Gel. *Langmuir* **2003**, *19*, 1254−1267.
(39) Ottiger, S.; Pini, R.; Storti, G.; Mazzotti, M. Measuring and Modeling the Competitive Adsorption of CO_2, CH_4, and N_2 on a Dry Coal. *Langmuir* **2008**, *24*, 9531−9540.
(40) Sudibandriyo, M.; Mohammad, S. A.; Robinson, R. L.; Gasem, K. A. M. OnoKondo Model for High-Pressure Mixed-Gas Adsorption on Activated Carbons and Coals. *Energy Fuels* **2011**, *25*, 3355−3367.
(41) Qajar, A.; Daigle, H.; Prodanovi, M. Methane dual-site adsorption in organic-rich shale-gas and coalbed systems. *International Journal of Coal Geology* **2015**, *149*, 1−8.
(42) Kargbo, D. M.; Wilhelm, R. G.; Campbell, D. J. Natural Gas Plays in the Marcellus Shale: Challenges and Potential Opportunities. *Environ. Sci. Technol.* **2010**, *44*, 5679−5684.
(43) *U.S. Crude Oil and Natural Gas Proved Reserves, Year-End 2018*; Report for EIA, 2019.
(44) Liang, C.; Jiang, Z.; Zhang, C.; Guo, L.; Yang, Y.; Li, J. The shale characteristics and shale gas exploration prospects of the Lower Silurian Longmaxi shale, Sichuan Basin, South China. *Journal of Natural Gas Science and Engineering* **2014**, *21*, 636−648.
(45) Yang, R.; He, S.; Hu, Q.; Sun, M.; Hu, D.; Yi, J. Applying SANS technique to characterize nano-scale pore structure of Longmaxi shale, Sichuan Basin (China). *Fuel* **2017**, *197*, 91−99.
(46) Andrews, I. J. *The Carboniferous Bowland Shale gas study: geology and resource estimation*; Report for British Geological Survey, 2013.

https://doi.org/10.1021/acs.energyfuels.1c03723
Energy Fuels 2022, 36, 3443−3456

(47) Fauchille, A. L.; Ma, L.; Rutter, E.; Chandler, M.; Lee, P. D.; Taylor, K. G. An enhanced understanding of the Basinal Bowland shale in Lancashire (UK), through microtextural and mineralogical observations. *Marine and Petroleum Geology* **2017**, *86*, 1374−1390.
(48) Delle Piane, C.; Bourdet, J.; Josh, M.; Clennell, M. B.; Rickard, W. D. A.; Saunders, M.; Sherwood, N.; Li, Z.; Dewhurst, D. N.; Raven, M. D. Organic matter network in post-mature Marcellus Shale: Effects on petrophysical properties. *AAPG Bulletin* **2018**, *102*, 2305−2332.
(49) Delle Piane, C.; Ansari, H.; Li, Z.; Mata, J.; Rickard, W.; Pini, R.; Dewhurst, D. N.; Sherwood, N. Influence of organic matter type on porosity development in the Wufeng-Longmaxi Shale: A combined microscopy, neutron scattering and physisorption approach. *International Journal of Coal Geology* **2022**, *249*, 103880.
(50) Ansari, H.; Joss, L.; Hwang, J.; Trusler, J. P. M.; Maitland, G.; Pini, R. Supercritical adsorption in micro- and meso-porous carbons and its utilisation for textural characterisation. *Microporous Mesoporous Mater.* **2020**, *308*, 110537.
(51) Hwang, J.; Pini, R. Supercritical CO_2 and CH_4 Uptake by Illite-Smectite Clay Minerals. *Environ. Sci. Technol.* **2019**, *53*, 11588−11596.
(52) Span, R.; Wagner, W. A New Equation of State for Carbon Dioxide Covering the Fluid Region from the TriplePoint Temperature to 1100 K at Pressures up to 800 MPa. *J. Phys. Chem. Ref. Data* **1996**, *25*, 1509−1596.
(53) Setzmann, U.; Wagner, W. A New Equation of State and Tables of Thermodynamic Properties for Methane Covering the Range from the Melting Line to 625 K at Pressures up to 100 MPa. *J. Phys. Chem. Ref. Data* **1991**, *20*, 1061−1155.
(54) Cychosz, K. A.; Guillet-Nicolas, R.; Garca-Martnez, J.; Thommes, M. Recent advances in the textural characterization of hierarchically structured nanoporous materials. *Chem. Soc. Rev.* **2017**, *46*, 389−414.
(55) Ustinov, E. A.; Do, D. D.; Herbst, A.; Staudt, R.; Harting, P. Modeling of Gas Adsorption Equilibrium over a Wide Range of Pressure: A Thermodynamic Approach Based on Equation of State. *J. Colloid Interface Sci.* **2002**, *250*, 49−62.
(56) Thommes, M.; Kaneko, K.; Neimark, A. V.; Olivier, J. P.; Rodriguez-Reinoso, F.; Rouquerol, J.; Sing, K. S. W. Physisorption of gases, with special reference to the evaluation of surface area and pore size distribution (IUPAC Technical Report). *Pure Appl. Chem.* **2015**, *87*, 1051.
(57) Zeng, J.; Jia, W.; Peng, P.; Guan, C.; Zhou, C.; Yuan, X.; Chen, S.; Yu, C. Composition and pore characteristics of black shales from the Ediacaran Lantian Formation in the Yangtze Block, South China. *Marine and Petroleum Geology* **2016**, *76*, 246−261.
(58) Linstrom, P.; Mallard, W. *NIST Chemistry WebBook, NIST Standard Reference Database Number 69*; 20899; National Institute of Standards and Technology: Gaithersburg MD, 2022.



https://doi.org/10.1021/acs.energyfuels.1c03723
Energy Fuels 2022, 36, 3443−3456